Identification of the Norton-Green Compaction Model for the Prediction of the Ti-6Al-4V Densification During the Spark Plasma Sintering Process

Charles Manière, Ugras Kus, Lise Durand, Ronan Mainguy, Julitte Huez, Denis Delagnes, Claude Estournès

Identification of the Norton-Green Compaction Model for the Prediction of the Ti–6Al–4V Densification During the Spark Plasma Sintering Process**

By *Charles Manière, Ugras Kus, Lise Durand, Ronan Mainguy, Julitte Huez, Denis Delagnes* and *Claude Estournès**

One of the main challenges for the industrialization of the spark plasma sintering (SPS) is to resolve issues linked to the compaction of real parts with complex shapes. The modeling of powder compaction is an interesting tool to predict how the densification field varies during sintering. However, expressing the behavior law which reflect the powder compaction is often a difficult and long step in the model establishment. In this paper, a simple methodology for the identification of the densification parameters is proposed. Dense and porous creep tests combined with SPS die compaction tests are employed to determine a complete densification law on a Ti–6Al–4V alloy directly in a SPS machine. The compaction model obtained is successfully validated through prediction of the densification of new SPSed samples.

1. Introduction

The spark plasma sintering process is a breakthrough technology based on the simultaneous application of high pressure and high temperature. This process is close to hot pressing (HP) except that the heat is generated, both in the tools and sample if electrically conducting, by a pulsed current applied through the entire column.[1] This process yields high temperatures and pressures, respectively, up to 2 000 °C and 150 MPa (with graphite tools) and a rapid heating rate (up to 1 000 °C min^{-1}). This technology can produce a wide range of highly dense materials from polymers, metals, and alloys including refractory materials and is a promising technique to obtain better-controlled and homogeneous microstructures.[2] Despite all these advantages, it is difficult to predict and control the temperature and densification field during the experiment. To avoid long and expensive trial-and-error experiments, finite element modeling (FEM) can be a very powerful tool.

Two main phenomena are usually modeled: Joule heating and sintering. Concerning the electro-thermal part (heating), many authors consider the pure resistive model to be a good approximation of the heating phenomena.[3–6] They point out the concentration of heat in the punches and the important effect of electric and thermal contacts[7–12] on the temperature field. On the other hand, the powder compaction phenomenon is often modeled using the visco-plastic approach through Olevsky,[13,14] Abouaf,[15] or Camclay[16] models. This approach requires the identification of creep laws on both the dense and the porous material. In a classical approach, the identification of the creep parameters is particularly long and difficult and needs compression experiments at different temperatures and pressures with dense and porous material samples. Instrumented hot isostatic pressing (HIP) tests also have to be performed,[17,18] they generally need very long heating times (i.e., several hours) compared to our target SPS process (a few minutes). The impact of the heating time on the microstructure can be potentially high and cause discrepancies in the model. Consequently, an increasingly number of

[*] *Dr. C. Estournès, Dr. C. Manière, U. Kus*
CIRIMAT, Université de Toulouse, CNRS, INPT, UPS 118 route de Narbonne, 31062 Toulouse cedex 9, France
E-mail: estournes@chimie.ups-tlse.fr
Dr. C. Manière, Dr. L. Durand
CEMES, CNRS UPR 8011 and Université de Toulouse, 29 rue Jeanne Marvig, 31055 Toulouse, France
U. Kus, R. Mainguy, Dr. J. Huez
CIRIMAT, Université de Toulouse, CNRS, INPT, UPS 4 allée Emile Monso, 31030 Toulouse cedex 4, France
Dr. D. Delagnes
Université de Toulouse, CNRS, Mines Albi, INSA, UPS, ISAE, ICA (Institut Clément Ader), Campus Jarlard, 81013 Albi, France

[**] *The support of the Plateforme Nationale CNRS de Frittage Flash (PNF2/CNRS) is gratefully appreciated. C. M. and C. E. thank the French National Research Agency (ANR) for financial support of this study within project ANR09 MAPR-007 Impulsé.*

authors use inverse analysis to determine the powder compaction parameters directly on the SPS tests.[14–20] Other authors substitute HIP tests by another type of mechanical test such as the determination of the radial strain rate in a cylindrical porous creep test,[21] or a die compaction test.[22,23] In the present work, a methodology is proposed to determine the powder compaction parameters for the Norton-Green model[24] also called the Abouaf model. The method developed includes creep and SPS die compaction tests similar to that reported by Geindreau et al.[23] The method is applied to SPS machine using different configurations. These creep and die compaction configurations and operational conditions were improved in order to obtain a good stability of the temperature and accurate results.

The main contribution of this work is then to adapt the classical methodology[15–23] to the SPS conditions (high heating rate and pressure) in the aim of being very close to the target application of the model. The proposed methodology is then perfectly suited to determine densification properties for potential applications using fine microstructures or for a preserved specific phase or microstructures.

The identification process is divided into two steps: i) creep experiments are performed by direct/indirect heating of cylindrical samples of dense material at different temperatures (current assisted or current insulated). ii) the determination of the compaction law is performed using the results obtained from creep tests with cylindrical samples of porous material and SPS die compaction tests.

In this paper, the densification of the Ti–6Al–4V alloy also call TA6V is investigated. This alloy is widely used in aerospace applications,[25,26] due to its low density and its good mechanical properties at high temperature (up to 400 °C).[27–29] Moreover, this alloy is also used for medical applications due to its bio-compatibility.[2,30]

2. Experimental Section

All the experiments were performed on the SPS machine (Dr. Sinter 2080, SPS Syntex Inc, Japan) of the "Plateforme Nationale CNRS de Frittage Flash" located at the Université Toulouse III-Paul Sabatier. For this study, the densification behavior of a Ti–6Al–4V alloy was investigated with dense samples produced by die forging (for more details see a previous study[31,32]), and a prealloyed powder kindly provided by Aubert and Duval. This powder is made of spherical granules ranging in size from 40 to 400 μm. An SEM image and the composition of the powder are given in Figure 1 and Table 1, respectively. In the following, when we refer to the cast material we will speak about dense Ti–6Al–4V, otherwise we are referring to the powder material.

For the identification of the densification model different experimental configurations reported in Figure 2 were used. The determination of creep behavior on dense samples was performed using the configurations reported in Figure 2a and b. The determination of the powder compaction behavior

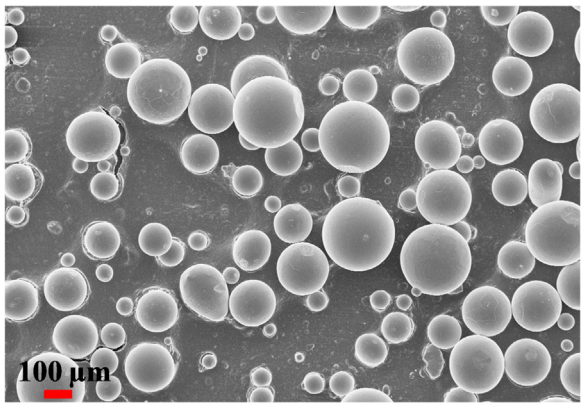

Fig. 1. Ti–6Al–4V powder under the Scanning Electron Microscope (SEM).

requires two types of experiment: i) creep experiments on porous samples as reported in Figure 2c and powder SPS die compaction experiments using the configuration reported in Figure 2d.

The creep experiments were performed on dense Ti–6Al–4V cylinders 8 mm in diameter and 10 mm in height. Two different configurations, reported in Figure 2a and b, were used to carry out these experiments:

Configuration 1, direct heating creep tests (Figure 2a): the current is allowed to pass through the sample.

Configuration 2, indirect heating creep tests (Figure 2b): the current passes only through the die that is added to heat the sample. For this configuration the sample is electrically insulated by a boron nitride spray deposited on the upper and lower punch faces in contact with the sample. For the porous creep experiments, a similar configuration was used (Figure 2c) except the sample was a porous cylinder obtained by interrupted SPS compaction. The last configuration (Figure 2d) is SPS die compaction performed on the powder inserted into an 8 mm inner diameter graphite die.

The creep tests (Figure 2a–c) were performed at different holding temperatures between 750 and 900 °C at a heating rate of 100 K min^{-1}. Except for the contact due to the thermal expansion of the cylinder, only a minimum load was applied during the heating ramp. Then only a few MPa are applied before the isothermal stage. Once the temperature setpoint is reached and the thermal expansion is stabilized, different levels of pressure were applied and the dwell time for each was maintained until stabilization of the strain rate. The SPS die compaction experiment (Figure 2d) was performed at a given temperature ($T = 820$ °C) with different levels of applied pressure until complete densification of the powder. The

Table 1. Chemical composition of the Ti–6Al–4V powder.

Element	Al	V	Fe	C	N	O	Ti
[%wt]	6.12	4.06	0.19	0.014	0.003	0.15	Base

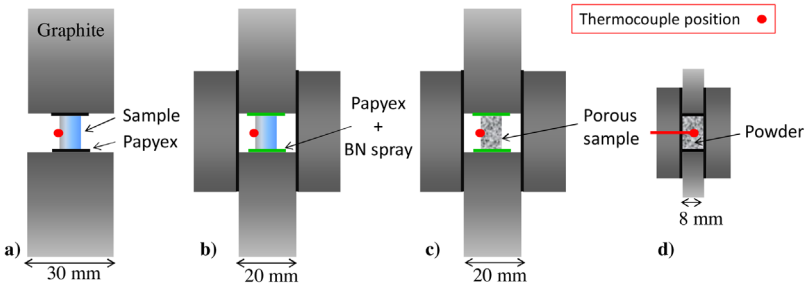

Fig. 2. Creep and compaction test configurations: (a) direct heating creep of dense samples (current assisted), (b) indirect heating creep of dense samples (current insulated), (c) indirect heating creep of porous samples, (d) classical SPS test (SPS die compaction test).

temperature measurements were performed by a K-type thermocouple positioned in contact to the surface of the sample for the experiments reported in Figure 2a–c. A 1 mm deep hole is previously made at the surface of the sample to maintain the thermocouple during the shrinkage. For the experiment corresponding to Figure 2d, the temperature is obtained by a K-type thermocouple placed directly in the powder bed. Another experiment was performed to ensure that the thermocouple does not disturb the measurement of the shrinkage curve.

To check the model (creep and densification), two experiments (configuration displayed in Figure 2d) were performed up to stabilization of the relative density at a constant applied pressure of 25 MPa and with two temperature ramps: i) 50 and ii) 100 K min^{-1}. These compaction tests were repeated twice to determine the temperature of the sample (by another thermocouple placed in the powder bed) and the displacement of the graphite thermal expansion in the anisothermal part.

3. Theory and Calculation

3.1. Compressive Dense Creep Formulation

The Norton-Green model is based on a creep power law formula defined for visco-plastic materials.

$$\dot{\varepsilon}_{eq} = A\sigma_{eq}^{n} \tag{1}$$

where $\dot{\varepsilon}_{eq}$ is the equivalent strain rate (s^{-1}), σ_{eq} the equivalent stress (Pa) and A a temperature dependent parameter (s^{-1} Pa^{-n}):

$$A = A_0 \exp\left(\frac{-Q}{RT}\right) \tag{2}$$

with, A_0 the pre-exponential factor (s^{-1} Pa^{-n}), R the universal gas constant (J mol^{-1} K^{-1}), Q the creep activation energy (J mol^{-1}) and T the absolute temperature.

The A and n Norton parameters are identified using compressive creep tests (Figure 2a and b) with the following linear regression equation:

$$\ln\ \dot{\varepsilon}_{eq}\ = \ln(A) + n\ln\ \sigma_{eq} \tag{3}$$

The experimental strain rate can be calculated with the true strain expression:

$$\dot{\varepsilon} = \frac{d\left(\ln\left(\frac{h}{h_0}\right)\right)}{dt} \tag{4}$$

with, h_0 and h, respectively, the initial and at the given time heights of the cylindrical sample.

The experimental stress can be calculated with the measured force and the sample section S. The section can be determined each time increment by the height h and the initial section S_0 of the sample assuming conservation of the cylindrical shape.

$$S = S_0 \frac{h_0}{h} \tag{5}$$

3.2. Norton-Green Model Description

The strain rate tensor of the Norton-Green model for porous solids is as follows[17]:

$$\underline{\dot{\varepsilon}} = A\sigma_{eq}{}^{n-1}\left(\frac{3}{2}c\underline{s} + fI_1\ \mathbb{i}\right) \tag{6}$$

with, $\underline{s}$ the deviatoric stress tensor, I_1 the stress tensor first invariant (the trace of the stress tensor), $\mathbb{i}$ the identity tensor, c and f functions of the relative density ρ.[24]

The equivalent stress is defined by the following equation:

$$\sigma_{eq} = \sqrt{3cJ_2 + fI_1^2} \tag{7}$$

with, J_2 the deviatoric stress tensor second invariant.

Developing the expression of the deviatoric stress tensor $\underline{s}$ in (6) gives the stress tensor expression as follows:

$$\underline{\sigma} = A^{-\frac{1}{n}}\dot{\varepsilon}_{eq}{}^{\frac{1}{n}-1}\left(\frac{2}{3c}\underline{\dot{\varepsilon}} + \left(\frac{1}{9f} - \frac{2}{9c}\right)tr(\underline{\dot{\varepsilon}})\ \mathbb{i}\right) \tag{8}$$

This expression is close to the expression used in the Olevsky model in a pure visco-plastic approach[13]:

The equivalent strain rate is defined by the following equation:

$$\dot{\varepsilon}_{eq} = \sqrt{\frac{2}{3c}\underline{\dot{\varepsilon}} : \underline{\dot{\varepsilon}} + \left(\frac{1}{9f} - \frac{2}{9c}\right)tr(\underline{\dot{\varepsilon}})^2} \tag{9}$$

To link the variation of the relative density ρ and the local volume change, mass conservation is defined as follows:

$$\frac{\dot{\rho}}{\rho} = -tr(\underline{\dot{\varepsilon}}) \tag{10}$$

3.3. Compressive Porous Creep Formulation

The macroscopic stress tensor in compressive creep with a porous sample (Figure 2c) can be reduced to:

$$\underline{\sigma} \equiv \begin{pmatrix} 0 & 0 & 0 \\ 0 & 0 & 0 \\ 0 & 0 & \sigma_z \end{pmatrix} \tag{11}$$

with, z the revolution axis of the cylindrical sample.

The expression of the equivalent stress (7) can be reduced to:

$$\sigma_{\text{eq}} = |\sigma_z|\sqrt{c+f} \tag{12}$$

Combining (12), (11), and (6) we obtain the first c and f identification expression for the porous creep tests (Figure 2c):

$$|\dot{\varepsilon}_z| = A(f+c)^{\frac{n+1}{2}}|\sigma_z|^n \tag{13}$$

3.4. SPS Powder Die Compaction

The SPS case can be assimilated to uniaxial compaction, along the z-axis, of the powder in the die. Then the macroscopic strain rate tensor can be reduced to:

$$\underline{\dot{\varepsilon}} \equiv \begin{pmatrix} 0 & 0 & 0 \\ 0 & 0 & 0 \\ 0 & 0 & \dot{\varepsilon}_z \end{pmatrix} \tag{14}$$

The equivalent strain rate (9) is then given by the relation:

$$\dot{\varepsilon}_{eq} = |\dot{\varepsilon}_z|\frac{1}{3}\sqrt{\frac{4}{c}+\frac{1}{f}} \tag{15}$$

Combining (15), (14), and (8) we obtain the second c and f identification expression for the SPS die compaction tests (Figure 2d):

$$|\sigma_z| = A^{-\frac{1}{n}}|\dot{\varepsilon}_z|^{\frac{1}{n}}\left(\frac{1}{3}\right)^{\frac{1-n}{n}}\left(\frac{4}{c}+\frac{1}{f}\right)^{\frac{n+1}{2n}}\frac{1}{9} \tag{16}$$

3.5. c and f Identification Equations

The c and f functions can then be determined by the resolution of the following system of two equations (17). $c+f$ was obtained from porous creep tests (with configuration Figure 2c) and $4/c+1/f$ from SPS die compaction tests (with configuration Figure 2d):

$$\begin{cases} c+f = \left(\dfrac{|\dot{\varepsilon}_z|}{A|\sigma_z|^n}\right)^{\dfrac{2}{n+1}} \\ \dfrac{4}{c}+\dfrac{1}{f} = \left(9A^{\frac{1}{n}}|\sigma_z||\dot{\varepsilon}_z|^{-\frac{1}{n}}\left(\dfrac{1}{3}\right)^{-\frac{1-n}{n}}\right)^{\dfrac{2n}{n+1}} \end{cases} \tag{17}$$

To summarize, five parameters have to be determined in order to model powder compaction. The parameters A_0, Q, and n for the power law creep were determined from creep tests on dense samples, and the c and f functions were determined from both creep and SPS die compaction tests on porous samples.

4. Results and Discussion

Sections 4.1 and 4.2 are devoted to the determination of the creep power law parameters A_0, Q, and n with the direct (Figure 2a) and indirect (Figure 2b) heating configurations. The identification of c and f is developed in Section 4.3. Section 4.4 is devoted to the validation of the powder compaction model with independent SPS tests.

4.1. Power Law Creep Identification in Direct Heating Configuration

The experimental curves of strain rate for increasing applied load obtained at 750 °C are reported in Figure 3a. An external camera is added for this experiment to verify the accuracy of the displacement curves provided by the SPS machine and to control that the eventual disturbance of the thermal expansion due to thermal non-equilibrium remains sufficiently low. The strain rate curves (camera vs. SPS) reported in Figure 3a in isothermal regime are very close. The SPS data are then acceptable meaning the thermal equilibrium is quickly reached or the temperature is sufficiently stable to allow displacement measurements. The experimental data points of the strain rate as a function of the stress rate obtained for temperatures of 750, 800, 850, and 900 °C are reported in a log-log graph (Figure 3b).

Considering Equation 3 for each temperature, the experimental points should naturally align on a straight line giving a slope that allows the n exponent to be determined. Regarding Figure 3, there is a high level of scattering in all of these curves, giving n values between 1 and 3 with an average value of 2.3. According to the Norton-Green model (Eq. 3), the experimental curves are expected to be roughly linear and positioned from the right (high pressure) for the low temperatures to the left (low pressure) for the high temperatures. These results show an inappropriate positioning of the curves, for instance the curve at 800 °C is expected to be on the left of the curves obtained at 750 °C. Moreover, the repeatability in the curves positioning at a single temperature of 750 °C is not satisfactory. This problem of positioning can be explained by the pictures of the sample, reported in Figure 3c, taken during a creep experiment at the beginning and the end of the isothermal dwell time. A strong thermal gradient was observed between the center of the cylindrical sample (hot) and the edge in contact with the punches (cool). This thermal gradient implies a higher deformation of the sample at his center and creates a non-cylindrical deformed sample at the end of the dwell. This phenomenon of thermal gradient can be explained by the output heat flux on the sample/punch interface that is strongly influenced by the

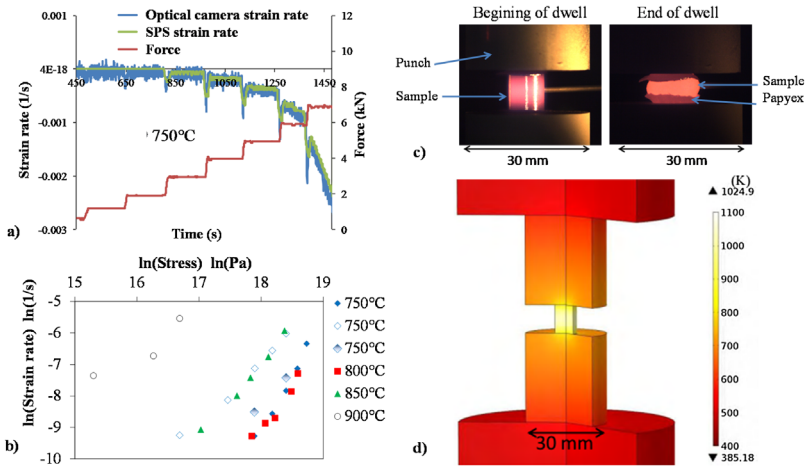

Fig. 3. Direct heating creep tests: (a) evolution of the strain rate curves for increasing applied loads obtain at 750 °C by the SPS device and with an external optical camera, (b) isobaric isotherm experimental points at 750, 800, 850, 900 °C; (c) images of a sample at the beginning and after dwell for the creep test (750 °C), (d) temperature profile simulated at the beginning of the dwell.

thermal contact resistance (TCR) of this interface. The less the pressure is, more is this TCR. Consequently, for a lower pressure, the TCR is higher and the output heat flux at the interface is lower, the overall temperature of the sample is then higher. In practical terms, this could explain why one of the curves at 750 °C was positioned on the left (higher overall temperature) for lower pressure as compared to the others.

Based on our previous work[11] on the Joule heating simulation of the spark plasma sintering, the maximum magnitude of the thermal gradient of the sample in direct configuration can be investigated numerically. The temperature dependent parameters of the SPS column elements are taken from ref.[11] except for the properties of Ti–6Al–4V which are reported in Table 2. At the specimen/punch contact, the thermal effect of the papyex on the specimen thermal gradient is a key parameter. As previously explained, the thermal contact resistance decreases the heat flow across the interface and then decreases the specimen thermal gradient. In order to evaluate the maximum magnitude of the specimen thermal gradient, the papyex effect is modeled by an interface condition that takes into account the 4 W $(m K)^{-1}$ thermal conductivity of the 0.2 mm papyex. The graphite/papyex and papyex/Ti–6Al–4V TCR, which decrease with the pressure and temperature, are thus taken equal zero. Considering a perfect TCR is then close to the case of high pressure and temperature and provides us a reasonable estimation of the specimen maximum temperature difference in that type of configuration. In accordance with the experimental picture (Figure 3c), the simulation picture reported in Figure 3d at the beginning of the dwell show a maximum temperature at the middle height of the specimen and an important decrease of the temperature in the area closed to the punch. The temperature difference is about 200 K. A simulation similar to the one presented in Figure 3d was also performed for a 5 mm height specimen and in that case the temperature difference is reduced to about 100 K. The temperature gradient is then significantly reduced for a smaller specimen height, but remains too high considering our tests. Moreover, considering the 1.8 mm of the thermocouple diameter, this configuration is too small to perform multi-step pressure creep tests that need more important shrinkage distances compare to the classical approaches.

The lack of control of the output heat flux prevents any identification of the creep parameters using this configuration. To solve this problem, in the next creep tests, an indirect heating configuration was developed where the heat is not generated in the sample but transferred from external elements in contact.

Table 2. Temperature-dependent properties of Ti–6Al–4V.[33]

Electrical resistivity (Ω m)	$1.35E\text{-}6 + 1.17E\text{-}9T\text{-}4.06E\text{-}13T^2$
Thermal conductivity (w $(m K)^{-1}$)	$8.11\text{-}0.0149T + 4.47E\text{-}5T^2\text{-}2.27E\text{-}8T^3$
Specific heat (J $(kg K)^{-1}$)	$383 + 0.671T\text{-}5.35E\text{-}4T^2 + 1.64E\text{-}7T^3$
Density (kg m^{-3})	$4467\text{-}0.119T\text{-}1.28E\text{-}5T^2$

4.2. Power Law Creep Identification in Indirect Heating Configuration

With the indirect heating configuration (Figure 2b), according to the picture taken at the beginning of the isothermal stage (Figure 4a), the temperature distribution in the sample appears to be more homogeneous. The experimental data points (Figure 4b) confirm this tendency because of the correct relative position of each curve with respect to the experimental temperature and the regular gap between them. Pictures of the samples after the creep tests are reported in Figure 5. The deformed sample shape is closer to a cylinder with indirect heating than with a direct heating configuration (Figure 3). The barrel effect is minimized. Linear regression can then be performed and gives: $A_0 = 30.6\,s^{-1}\,Pa^{-n}$; $Q = 416\,kJ\,mol^{-1}$ and $n = 2$.

$$\dot{\varepsilon}_{eq} = 30.6 \times \exp\left(\frac{-4.16 \times 10^5}{RT}\right)\sigma_{eq}^2 \tag{18}$$

The value of n thus obtained is finally close to that determined using direct heating and is in good agreement with the tendency of the values reported in the literature[29–32] that decrease with temperature (Figure 4c).

4.3. Identification of c and f

As the creep power law of the dense sample is now determined, the c and f functions can be identified. The system of Equations 17 was solved using creep tests performed on porous samples and SPS die compaction tests that gave values of the right hand side of both equations. The results of these tests are reported in Figure 6 with the upper

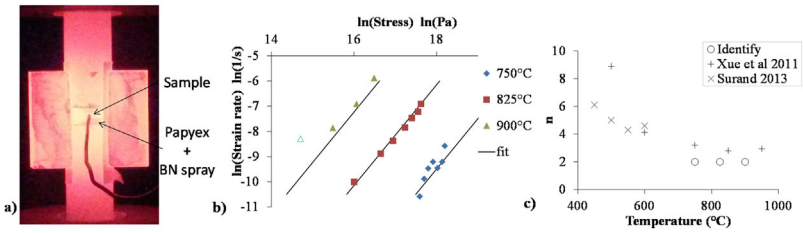

Fig. 4. Indirect heating creep tests: (a) picture of the heating at the beginning of the dwell, (b) linear regression with the isobaric isotherm experimental points at 750, 825, 900 °C, (c) the stress exponent n found in our study compared with those of the literature.

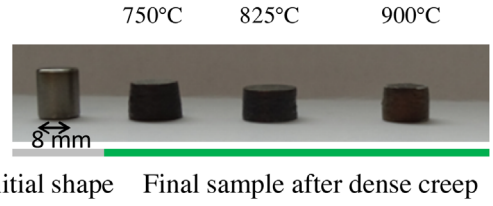

Fig. 5. Deformed samples after the creep experiments.

graph showing the data points of the porous creep test giving $c+f$ and of the SPS die compaction test giving $4/c+1/f$ for different relative densities. The resolution of the system (17) gives the two curves of c and f (Figure 6b and c).

$$c = 1 + 130 \times \left(\frac{1-\rho}{\rho - 0.2}\right)^{1.3} \tag{19}$$

$$f = 0.023 \times \left(\frac{1-\rho}{\rho - 0.67}\right)^{1.5} \tag{20}$$

At this point, all the parameters needed to model the compaction of the Ti–6Al–4V powder are determined. The following part of the paper is devoted to the validation of this model.

4.4. Model Validation

The results of two verification experiments performed at heating rates of 50 and 100 K min^{-1} with a constant applied pressure of 25 MPa are reported in Figure 7. These experiments are independent SPS die compaction tests. The comparison between experimental and calculated results shows a good agreement on almost all the Ti–6Al–4V densification curves whatever the slope of the temperature ramps. However, two small discrepancies were observed. In the low relative density part of the curve, there is a slight cold densification probably due to a plastic deformation of the powder granules not taken into account by the model. The other discrepancy is noticed in the final stage of both cycles. The relative density given by the model tends to reach the maximum value (complete densification) which is not the case for the experimental results. In ceramics, this kind of result can be explained by the high grain growth that occurs during the final stage.[34] The experimental non-attainment of the highest densification can also be explained by the great difference of the initial particle sizes that can produce large pores difficult to remove. In the present case, the Ti–6Al–4V sample presents a large distribution of the porosity size at the end of the sintering (see Figure 8a). The porosity is ranging from very large pore of 140 μm to small pores of 5 μm (see histogram Figure 8b). Another interesting point is the presence of thin and elongated pores near the large grains and oriented along the compaction direction. The removal of this porosity is more difficult because the thickness of this porosity is not oriented along the applied pressure direction. The shape of the porosity and its size distribution[35] seem to explain the sintering rate slowdown at the end of the sintering.

5. Conclusion

In this work we detailed a complete experimental methodology for the validation of the Norton-Green powder compaction model. One of its main advantages is that all the parameters of the creep constitutive law of the material can be easily determined using tests performed in an SPS machine and that it is not necessary to use instrumented HIP trials that

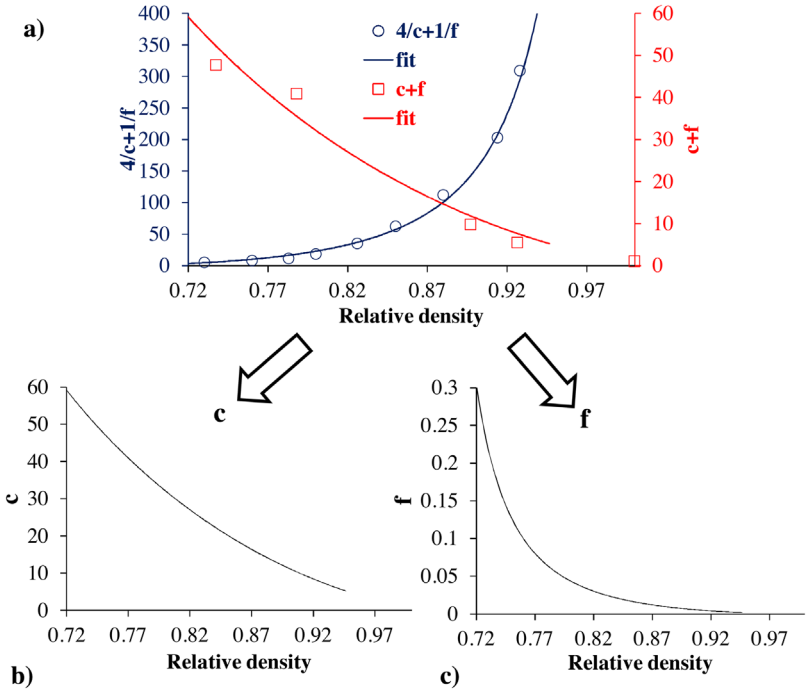

Fig. 6. Determination of c and f functions: (a) experimental points for the porous creep (c + f) and SPS die compaction (4/c 1/f); (b and c) are, respectively, c and f functions depending on the relative density.

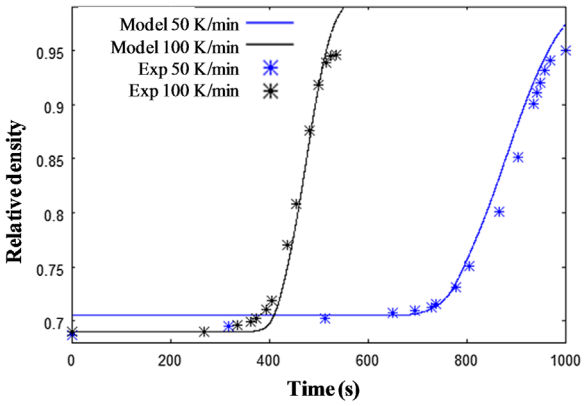

Fig. 7. Comparison of experimental/modeled relative density curves for 50 and 100 K min^{-1} at 25 MPa.

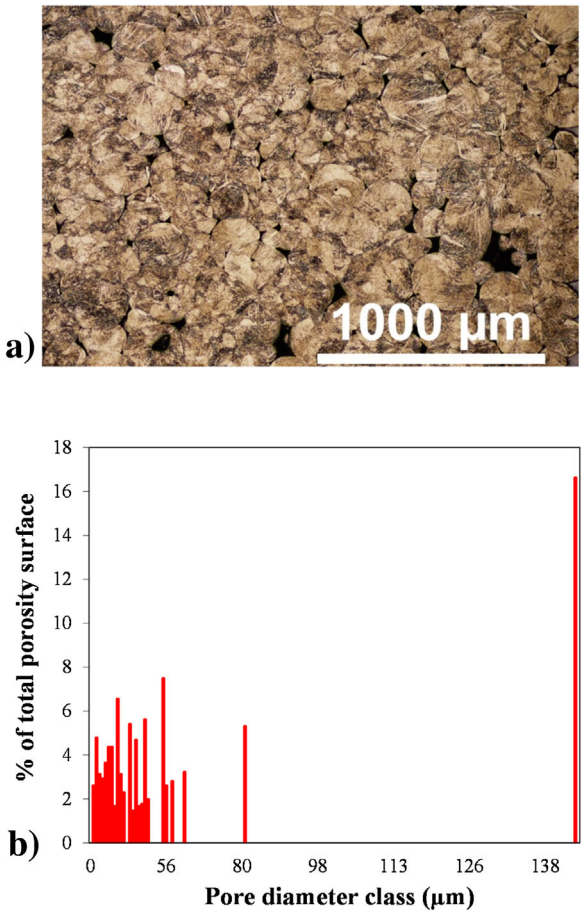

Fig. 8. (a) Typical polished surface microstructure of the spark plasma sintered samples, (b) porosity diameter repartition.

are generally long and difficult. This method requires compressive creep tests on both dense and porous samples and SPS die compaction tests.

For creep parameter determination, two configurations for sample heating were used. The direct heating configurations via the dc-pulsed current passing through the sample and then was rapidly abandoned. To solve this problem, another configuration by indirect heating of the sample was employed. Then, the temperature gradient was no longer observed in the sample and both dense and porous creep tests give satisfactory results. First, creep law (A_0, Q, and n) parameters for the dense sample were determined. Combining creep with SPS die compaction tests, it was possible to determine the c and f functions, in relation with the variations of the porous material during the densification. Finally, two verification tests to simulate the densification of a Ti–6Al–4V powder, using the creep parameters thus determined, showed really good agreement between the experimental and simulated variation of the relative density with temperature thus validating the overall methodology developed.

[1] Z. A. Munir, U. Anselmi-Tamburini, M. Ohyanagi, *J. Mater. Sci.* **2006**, *41*, 763.

[2] R. Orrù, R. Licheri, A. M. Locci, A. Cincotti, G. Cao, *Mater. Sci. Eng. R* **2009**, *63*, 127.

[3] K. Matsugi, H. Kuramoto, T. Hatayama, O. Yanagisawa, *J. Mater. Process. Technol.* **2003**, *134*, 225.

[4] U. Anselmi-Tamburini, S. Gennari, J. E. Garay, Z. A. Munir, *Mater. Sci. Eng. A* **2005**, *394*, 139.

[5] G. Molénat, L. Durand, J. Galy, A. Couret, *J. Metall.* **2010**, *2010*, 1.

[6] J. B. Allen, C. Walter, *ISRN Mater. Sci.* **2012**, *2012*, 1.

[7] A. Zavaliangos, J. Zhang, M. Krammer, J. R. Groza, *Mater. Sci. Eng. A* **2004**, *379*, 218.

[8] G. Maizza, S. Grasso, Y. Sakka, *J. Mater. Sci.* **2009**, *44*, 1219.

[9] K. Vanmeensel, A. Laptev, O. Van der Biest, J. Vleugels, *J. Eur. Ceram. Soc.* **2007**, *27*, 979.

[10] C. Manière, A. Pavia, L. Durand, G. Chevallier, V. Bley, K. Afanga, A. Peigney, C. Estournès, *Electr. Power Syst. Res.* **2015**, *127*, 307.

[11] C. Manière, A. Pavia, L. Durand, G. Chevallier, K. Afanga, C. Estournès, *J. Eur. Ceram. Soc.* **2015**, *36*, 741.

[12] C. Arnaud, C. Manière, G. Chevallier, C. Estournès, R. Mainguy, F. Lecouturier, D. Mesguich, A. Weibel, L. Durand, Ch. Laurent, *J. Mater. Sci.* **2015**, *50*, 7364.

[13] E. A. Olevsky, C. Garcia-Cardona, W. L. Bradbury, C. D. Haines, D. G. Martin, D. Kapoor, *J. Am. Ceram. Soc.* **2012**, *95*, 2414.

[14] C. Manière, L. Durand, A. Weibel, C. Estournès, *Acta Mater.* **2016**, *102*, 169.

[15] M. Abouaf, J. L. Chenot, G. Raisson, P. Bauduin, *Int. J. Numer. Methods Eng.* **1988**, *25*, 191.

[16] K. V. Ranjit, N. S. Mahesh, M. I. Anwar, *SAS Technol.* **2012**, *11*, 79.

[17] M. Abouaf, *Modélisation de la compaction de poudres métalliques frittées Approche par la mécanique des milieux continus*, PhD Thesis, L'institut national polytechnique de Grenoble **1985**.

[18] J. Besson, *Simulation numérique de la mise en forme des céramiques application à la compaction isostatique à chaud*, PhD Thesis, L'école nationale supérieure des mines de Paris **1990**.

[19] P. Mondalek, *Numerical Modeling of the Spark Plasma Sintering Process*, PhD Thesis, Ecole nationale supérieure des mines de Paris **2012**.

[20] X. Wei, C. Back, O. Izhvanov, O. Khasanov, C. Haines, E. Olevsky, *Materials* **2015**, *8*, 6043.

[21] E. Brisson, *Etude experimentale du frittage assemblage d un composite conducteur en Ag SnO2 sur un support en cuivre par courants pulses*, PhD Thesis, Université de Bretagne-Sud **2014**.

[22] C. Geindreau, D. Bouvard, P. Doremus, *Eur. J. Mech. A Solid* **1999**, *18*, 581.

[23] C. Geindreau, D. Bouvard, P. Doremus, *Eur. J. Mech. A Solid* **1999**, *18*, 597.

[24] R. J. Green, *Int. J. Mech. Sci.* **1972**, *14*, 215.

[25] R. R. Boyer, *Mater. Sci. Eng. A* **1996**, *213*, 103.

[26] L. Xu, R. Guo, C. Bai, J. Lei, R. Yang, *J. Mater. Sci. Technol.* **2014**, *30*, 1289.

[27] L. Badea, M. Surand, B. Viguier, J. Ruau, *U. P. B. Sci. Bull. Series B* **2014**, *76*, 185.

[28] X. Li, T. Sugui, B. Xianyu, C. Liqing, *Mater. Sci. Eng. A* **2011**, *529*, 452.

[29] Y. Xue, L. H. Lang, G. L. Bu, L. Li, *Sci. Sinter.* **2011**, *43*, 247.

[30] E. Mohseni, E. Zalnezhad, A. R. Bushroa, *Int. J. Adhes. Adhes.* **2014**, *48*, 238.

[31] C. Buirette, *Study of Mechanisms of Propagation of Cracks in an Titanium Alloy Welded by Electron Bean*. PhD Thesis, Institut National Polytechnique, Toulouse **2011**.

[32] M. Surand, Etude du comportement viscoplastique en traction et en fluage de l'alliage de TA6V de 20°C à 600°C. PhD Thesis, Université Toulouse III Paul Sabatier **2013**.

[33] http://www.matweb.com/ (**2016**).

[34] C. Manière, L. Durand, A. Weibel, C. Estournès, *Ceram. Int.* **2016**, *42*, 9274.

[35] R. German, *Sintering Theory and Practice*, Wiley, New York **1996**.